



Boosting holes generation and O₂ activation by bifunctional NiCoP modified Bi₄O₅Br₂ for efficient photocatalytic aerobic oxidation

Weijie Yang^a, Kailong Sun^a, Jun Wan^{a,*}, Yang-Ai Ma^a, Jiaqing Liu^a, Bicheng Zhu^{b,*}, Lin Liu^{a,*}, Feng Fu^{a,*}

^a College of Chemistry & Chemical Engineering, Yan'an University, Research Institute of Comprehensive Energy Industrial Technology, Shaanxi Key Laboratory of Chemical Reaction Engineering, Clean Utilization of Low Rank Coal of Shaanxi Collaborative Innovation Center, Yan'an 716000, China

^b Laboratory of Solar Fuel, Faculty of Materials Science and Chemistry, China University of Geosciences, Wuhan 430074, China

ARTICLE INFO

Keywords:

Photocatalytic aerobic oxidation
Oxidative active species
Transition metal phosphides
S-scheme
Oxygen activation

ABSTRACT

The insufficient generation of oxidative active species severely limits the activity of photocatalytic aerobic oxidation for organic pollutants degradation in wastewater. Herein, transition metal phosphides (TMPs) cocatalysts, including Ni₂P, Co₂P, and NiCoP, were loaded on Bi₄O₅Br₂ nanosheets by a simple liquid assembly method. Among which, 15% NiCoP/Bi₄O₅Br₂ heterojunction exhibits the optimal photocatalytic activity for degrading phenolic pollutants owing to the high concentration of h⁺ and •O₂⁻ active species, and it displays excellent tolerance for the inorganic ions, pH value, water matrix, and outdoor sunlight. The S-scheme charge transfer mechanism was revealed for NiCoP/Bi₄O₅Br₂ heterojunction, which significantly improves the separation efficiency of photogenerated charge carriers and facilitates the accumulation of active h⁺. Furthermore, NiCoP with high reduction potential and outstanding O₂ activation ability is served as the active site for producing •O₂⁻. This work can inspire the further design of bifunctional photocatalysts for efficient photocatalytic aerobic oxidation applications.

1. Introduction

Along with the propulsion of petrochemical, coal, and pharmaceutical industries, large amounts of wastewater with noxious pollutants are discharged into the environment. Reducing the pollution load of the industry has significant implications for constructing an environment-friendly society. In particular, phenolic pollutants are persistent and non-biodegradable harmful organic substances, which are highly resistant to conventional wastewater treatment methods [1]. In recent years, photocatalytic aerobic oxidation technology with molecular oxygen (O₂) as an oxidant has attracted extensive attention in pollutants degradation for its green and high-efficiency properties [2–4]. Typically, the main oxidative active species in photocatalytic aerobic oxidation are the photogenerated holes (h⁺), superoxide radicals (•O₂⁻), and hydroxyl radicals (•OH) from the molecular oxygen (O₂) [5], etc.

Among various semiconductors, bismuth oxyhalide (Bi_mO_nX_p, X = Cl, Br, I) layered material with good chemical stability, visible-light response, and enough oxidation potential is a promising photocatalyst offering potential to overcome the limitation [6–8]. Nevertheless, the pristine

bismuth oxyhalide photocatalysts suffer from a high recombination rate of photogenerated electron-hole pairs, leading to a low concentration of photogenerated holes for the oxidation reaction. Moreover, the inadequate supply of •O₂⁻ radical by bismuth oxyhalide tremendously limits its catalytic activity, which is because of the insufficient reduction potential of the conduction band (CB) and the lack of the active sites for O₂ activation [9,10]. At present, the strategy mostly focuses on constructing heterojunction or cocatalytic systems, such as Bi₄O₅Br₂/Ti₃C₂ [11], AgCO₃/Bi₄O₅I/g-C₃N₄ [12], BiOBr/CdS [13], to increase the active charge concentration by promoting the electron-hole separation efficiency. However, the optimization of surface active sites for accelerating oxygen activation is in great deficiency, which impedes its practical applications. To this end, building a dual-functional catalytic system for simultaneously boosting the holes generation and oxygen activation remains a great challenge for increasing the photocatalytic performance of aerobic oxidation.

Transition metal phosphides (TMPs), such as Ni₂P and Co₂P, have been intensively investigated as non-precious metal cocatalysts in improving photocatalytic efficiency because of their outstanding

* Corresponding authors.

E-mail addresses: wanjun@yau.edu.cn (J. Wan), zhubicheng1991@163.com (B. Zhu), liulin_0731@163.com (L. Liu), yadxufeng@126.com (F. Fu).

<https://doi.org/10.1016/j.apcatb.2022.121978>

Received 16 July 2022; Received in revised form 28 August 2022; Accepted 10 September 2022

Available online 13 September 2022

0926-3373/© 2022 Elsevier B.V. All rights reserved.

conductivity and stability [14,15]. For instance, Wang et al. utilized the Ni₂P nanoparticles as an electron trap to facilitate the hole accumulation on g-C₃N₄ photocatalyst, remarkably improving its photocatalytic bacterial inactivation efficiency [16]. Besides, it is known that the oxygen molecule has two unpaired electrons in the π^*_{2px} and π^*_{2py} orbitals, which makes it susceptible to accepting electrons and forming reactive oxygen species [17]. Upon O₂ adsorption on the transition metal surfaces, the filled d-orbitals of the transition metal can be hybridized with the p orbitals in the oxygen atom, imparting electrons transfer from the metal to the adsorbed O₂ [18]. For example, Kong et al. reported the interaction of the p orbitals of an oxygen atom with d-orbitals of Au-Co dual atoms, which provides an encouraging way to design highly efficient electrocatalysts for acidic oxygen reduction [19]. Specifically, owing to the weak metal bond strength in TMPs, the surface metals of TMPs possess unique coordinatively unsaturated multielectronic properties, endowing it fantastic electron-donating and bonding ability as a reduction active site [20]. Meanwhile, considering TMPs are typically used as efficient catalysts toward hydrodesulfurization (HDS) to interact with sulfur species [21,22], they are also expected to be active for O₂ activation. However, no efforts so far have been focused on the O₂ activation effect of TMPs. Based on all the above considerations, it would be a promising strategy to employ TMPs as bifunctional co-catalysts with bismuth oxyhalide, the research is of great significance to develop a novel integrated modification for optimizing the photocatalytic aerobic oxidation performance.

In this work, we demonstrate the bifunctional effects of TMPs co-catalysts to accelerate the holes generation and O₂ activation simultaneously for the first time, and dual metal NiCoP displays a superior performance compared to the single metal phosphides of Ni₂P and Co₂P. Specifically, NiCoP/Bi₄O₅Br₂ heterojunction is designed for the photocatalytic degradation of phenolic pollutants. The experiment and DFT calculation results demonstrate the S-scheme charge transfer mechanism in the heterojunction to promote the charge separation efficiency and enhance the holes accumulation on Bi₄O₅Br. More importantly, NiCoP serves as an efficient catalytic site for the adsorption and activation of O₂ due to its sufficient reduction potential and negative adsorption energy. It is validated that more oxidative active species of photogenerated holes and superoxide radicals ($\bullet\text{O}_2^-$) are produced in the aerobic oxidation reaction, thus remarkably enhancing photocatalytic performance.

2. Experimental section

2.1. Materials

Bismuth nitrate pentahydrate (Bi(NO₃)₃·5 H₂O), potassium bromide (KBr), polyvinylpyrrolidone (PVP), ethanol, ethylene glycol, and ammonia solution (NH₃·H₂O) were purchased from Tianjin kemiu chemical reagent company (China). Nickel(II) chloride hexahydrate (NiCl₂·6 H₂O), cobalt chloride hexahydrate (CoCl₂·6 H₂O), and sodium dodecylbenzenesulfonate (SDBS) were purchased from Sinopharm chemical reagent corporation. Phosphorus red (RP), hexadecyltrimethylammonium chloride (CTAB), nitrotetrazolium blue chloride (NBT), bisphenol A (BPA), p-tert-Butylphenol (PTBP), 2, 4-dichlorophenol (2,4-DCP), phenol, isopropanol (IPA), ammonium oxalate (AO) and p-benzoquinone (BQ) were purchased from Aladdin industrial corporation. All chemicals were of analytical grade and were used without any further purification.

2.2. Synthesis of Bi₄O₅Br₂ nanosheet

Typically, 5 mmol of Bi(NO₃)₃·5 H₂O was firstly dispersed into 40 mL of ethylene glycol under magnetic stirring for 30 min. Then 5 mmol KBr were mixed over the solution and stirred for 30 min. After that, the mixed solution of 8 mL H₂O and 12 mL NH₃·H₂O was slowly added dropwise into the above solution and stirred for 4 h at room

temperature. Next, the suspension was transferred into a Teflon-lined autoclave and maintained at 140 °C for 20 h. Subsequently, the resulting precipitation was collected, washed using deionized water and ethanol several times, and finally dried at 60 °C overnight.

2.3. Synthesis of Ni₂P, Co₂P, and NiCoP nanoparticles

The commercial RP after the mill was firstly dispersed in deionized water for hydrothermal treatment at 200 °C for 12 h to reduce the particle size [23]. Subsequently, 0.5 mmol NiCl₂·6 H₂O and 0.5 mmol CoCl₂·6 H₂O were dissolved in the 50 mL mixed solution of deionized water and ethylene glycol (V/V=1:1), then 10 mmol treated RP, 0.1 g CTAB and 0.1 g SDBS were added into above solution under stirring for 30 min. The obtained suspension was transferred into a 100 mL Teflon-lined autoclave and heated at 200 °C for 12 h. After cooling down to room temperature, the black precipitate was separated by centrifugation and washed with deionized water and ethanol three times, the product was dried in a vacuum at 60 °C overnight to obtain NiCoP nanoparticles.

The Ni₂P nanoparticles were prepared similarly, except that 1 mmol of NiCl₂·6 H₂O is used and the hydrothermal temperature is about 140 °C. In addition, Co₂P nanoparticles were synthesized with 1 mmol of CoCl₂·6 H₂O and 15 mmol of treated RP.

2.4. Synthesis of TMPs/Bi₄O₅Br₂ photocatalysts

A series of TMPs/Bi₄O₅Br₂ photocatalysts with the different weight ratios of TMPs (Ni₂P, Co₂P, and NiCoP) were prepared by a directed liquid assembly strategy, which were denoted as x% TMPs/Bi₄O₅Br₂ (x % = 5%, 10%, 15%, and 20%). In a typical process, 0.2 g of Bi₄O₅Br₂ and some TMPs powder were dispersed in 15 mL ethylene glycol and stirred for 20 min, respectively. Then the solutions were sonicated for another 15 min to get completely uniform suspensions. Subsequently, the suspension of TMPs nanoparticles was dropwise into the above Bi₄O₅Br₂ suspension under an ultrasonic bath for 15 min. After that, the mixed liquid was continually stirred for 12 h. Finally, the samples were collected by suction filtration and dried in a vacuum at 60 °C overnight. Particularly, the Ni₂P/Bi₄O₅Br₂, Co₂P/Bi₄O₅Br₂, and NiCoP/Bi₄O₅Br₂ in the description of various characterizations refer to the samples of 15%.

2.5. Characterizations

Scanning electron microscopy (SEM) was conducted through a JEOL JSM-7600 F instrument. Transmission electron microscopy (TEM) images and elemental mapping were detected by a JEOL JEM-2100 F microscope. The X-ray powder diffraction (XRD) patterns of the samples were measured with a Shimadzu XRD-7000 powder diffractometer. The X-ray photoelectron spectroscopy (XPS) was measured with a Thermo Scientific ESCALAB 250Xi spectrometer. Electron paramagnetic resonance (EPR) signals of photogenerated holes and superoxide radicals were characterized by a Bruker300 spectrometer. O₂ temperature programmed desorption (TPD) was performed by using an AutoChem1 II 2920 chemisorption analyzer. The UV-vis diffuse reflectance spectra (DRS) were procured from a Shimadzu UV-2550 spectrophotometer. The photoluminescence (PL) spectra were captured on a Hitachi F-7000 fluorescence spectrometer. The photoelectrochemical performance of as-prepared samples was tested at the Chenhua CHI-660E electrochemical workstation with a standard three-electrode system. The degradation intermediates were determined by high-performance liquid chromatography-mass spectrometry (HPLC-MS, Orbitrap Fusion, Thermo, USA).

2.6. DFT theoretical calculation details

The density functional theory (DFT) calculations were carried out by using the Vienna Ab-initio Simulation Package (VASP). The exchange-

correlation interaction was described by generalized gradient approximation (GGA) with the PBE functional. The energy cutoff was set as 450 eV. The convergence threshold in geometry optimization was set as 10^{-5} eV for energy and 0.02 eV/Å for force. For the construction of surface models, a vacuum of 20 Å was used to eliminate interactions between periodic structures. The DFT-D method of Grimme was used to describe the van der Waals interaction.

2.7. Photocatalytic aerobic degradation experiment

The photocatalytic activity of the prepared samples was evaluated by the aerobic degradation of phenolic pollutants. Typically, 20 mg catalyst was dispersed in a bisphenol A (BPA) solution (20 mg/L, 100 mL), clean air was passed through the solution and the suspension was magnetically stirred in the dark for 30 min to achieve an adsorption-desorption equilibrium. Afterward, a 300 W Xe lamp with a UV cutting filter (0.33 W/cm^2 , $\lambda > 420 \text{ nm}$) was used as the irradiation source, and the solution is kept under magnetic stirring and air entrance. During the reaction, 3 mL aliquots of the solution were collected at 10 min intervals and filtered by 0.22 μm MCE membrane for analysis. The concentration of BPA was measured by Shimadzu UV-2600 spectrophotometer at the maximum absorption wavelength of 276 nm. Other phenolic pollutants including p-tert-butylphenol (PTBP), 2,4-dichlorophenol (2,4-DCP), and phenol were also employed to analyze the photocatalytic activity according to a similar procedure described above, but the degradation efficiency was tested every 30 min. The absorbances of PTBP and DCP pollutants were determined at wavelengths of 285 nm and 275 nm, and the concentration of phenol was detected by the colorimetric method at 507 nm, respectively. Moreover, the mineralization efficiency of phenolic pollutants was measured using a total organic carbon (TOC)

analyzer (Shimadzu TOC-LCPN Analyzer).

2.8. Capture experiments of oxidative active species

To investigate the oxidative active species in photocatalytic reaction, a series of controlled experiments using different scavengers were carried out under conditions similar to the photocatalytic degradation process. Specifically, 1 mmol/L of isopropanol (IPA), ammonium oxalate (AO), and p-benzoquinone (BQ) were added to capture hydroxyl radicals ($\bullet\text{OH}$), photogenerated holes (h^+), and superoxide radicals ($\bullet\text{O}_2^-$), respectively. Moreover, NBT with a maximum absorption peak at 259 nm was employed to detect the formation of $\bullet\text{O}_2^-$ by ultraviolet-visible spectrophotometer. The procedure was the same with the photodegradation experiments except that NBT (0.05 mM) replaced organic pollutants.

3. Results and discussion

3.1. Morphology and composition of photocatalysts

The morphology and microstructure of as-prepared samples were directly observed by SEM, TEM, and HRTEM. As shown in Fig. S1a–c, the $\text{Bi}_4\text{O}_5\text{Br}_2$ catalyst displays a typical nanosheet structure with a size of 100–300 nm, and the clear lattice fringes distance of 0.366 nm can be assigned to the (112) planes of $\text{Bi}_4\text{O}_5\text{Br}_2$ [24]. Besides, both Ni_2P , Co_2P , and NiCoP exhibit a morphology of nanoparticles below 20 nm (Fig. S1d–f). The TMPs/ $\text{Bi}_4\text{O}_5\text{Br}_2$ heterojunctions were synthesized along with the procedure as depicted in Fig. 1a, the SEM and TEM images of $\text{NiCoP}/\text{Bi}_4\text{O}_5\text{Br}_2$ are shown in Fig. 1b–d. It can be seen that the NiCoP nanoparticles are uniformly distributed on the surface of

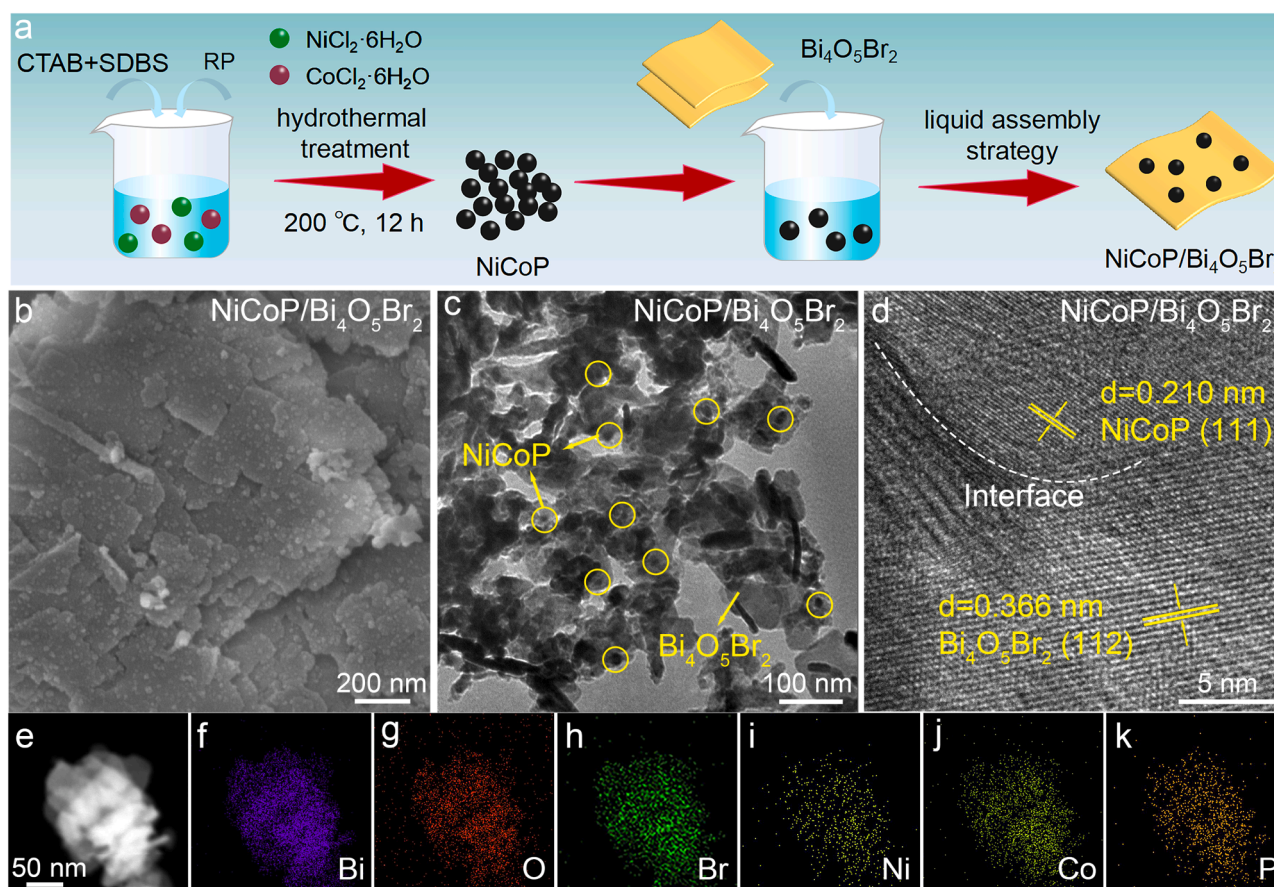


Fig. 1. (a) Schematic illustration for the synthesis of $\text{NiCoP}/\text{Bi}_4\text{O}_5\text{Br}_2$ photocatalyst. (b) SEM, (c) TEM, (d) HRTEM, (e) STEM and (f–k) corresponding EDX elemental mapping images of $\text{NiCoP}/\text{Bi}_4\text{O}_5\text{Br}_2$ photocatalyst.

$\text{Bi}_4\text{O}_5\text{Br}_2$ nanosheets with tight contact, the lattice fringes spacing of 0.210 and 0.366 nm are attributed to the (111) and (112) planes of hexagonal NiCoP and monoclinic $\text{Bi}_4\text{O}_5\text{Br}_2$ crystal, respectively [25]. Meanwhile, the STEM and EDX elemental mapping images (Fig. 1e–k) display the homogeneous distribution of Bi, O, Br, Ni, Co, and P elements in the $\text{NiCoP}/\text{Bi}_4\text{O}_5\text{Br}_2$ heterojunction. As exhibited in Figs. S2–3, $\text{Ni}_2\text{P}/\text{Bi}_4\text{O}_5\text{Br}_2$ and $\text{Co}_2\text{P}/\text{Bi}_4\text{O}_5\text{Br}_2$ nanocomposites show the same microstructure as the $\text{NiCoP}/\text{Bi}_4\text{O}_5\text{Br}_2$ sample, confirming the successful hybridization of TMPs nanoparticles with $\text{Bi}_4\text{O}_5\text{Br}_2$ nanosheet.

The crystal structure of the obtained photocatalysts was investigated by powder XRD. As displayed in Fig. S4a, the primary diffraction peaks of Ni_2P , Co_2P , and NiCoP samples are well-matched with the hexagonal Ni_2P (JCPDS No. 03–0953), orthorhombic Co_2P (JCPDS No. 32–0306) and hexagonal NiCoP (JCPDS No. 71–2336) [26–28], respectively. In addition, the diffraction peaks of $\text{Bi}_4\text{O}_5\text{Br}_2$ are well assigned to monoclinic $\text{Bi}_4\text{O}_5\text{Br}_2$ (JCPDS no. 37–0699) [29]. The TMPs/ $\text{Bi}_4\text{O}_5\text{Br}_2$ samples exhibit similar XRD patterns compared to the $\text{Bi}_4\text{O}_5\text{Br}_2$ (Fig. S4b), which is ascribed to the low concentration and weak crystallinity of TMPs nanoparticles. Besides, FTIR spectra were carried out to investigate the molecular structure of synthesized catalysts as illustrated in Fig. S4c. In detail, a sharp peak at 529 cm^{-1} can be observed in all the $\text{Bi}_4\text{O}_5\text{Br}_2$ and TMPs/ $\text{Bi}_4\text{O}_5\text{Br}_2$ catalysts, which belongs to the Bi–O stretching vibration for $[\text{Bi}_2\text{O}_2]^{2+}$ slabs [30]. After the introduction of TMPs, the new peak that appeared at 1068 cm^{-1} is assigned to the surface P–O group of TMPs [31], indicating the successful combination of TMPs with $\text{Bi}_4\text{O}_5\text{Br}_2$. Meanwhile, the peak at 1384 cm^{-1} might be attributed to residual ethyl alcohol [32], and the peaks at 1644 and 3452 cm^{-1} are due to the stretching and bending vibrations of surface-adsorbed water molecules [33]. Moreover, Fig. S4d presents the BET nitrogen adsorption/desorption isotherms of as-prepared catalysts. The specific surface areas of $\text{Bi}_4\text{O}_5\text{Br}_2$, $\text{Ni}_2\text{P}/\text{Bi}_4\text{O}_5\text{Br}_2$, $\text{Co}_2\text{P}/\text{Bi}_4\text{O}_5\text{Br}_2$, and $\text{NiCoP}/\text{Bi}_4\text{O}_5\text{Br}_2$ are measured to be $28.33\text{ m}^2/\text{g}$, $27.11\text{ m}^2/\text{g}$, $28.47\text{ m}^2/\text{g}$, and $24.81\text{ m}^2/\text{g}$, respectively. The result indicates that the introduction of TMPs has little effect on the specific surface area of catalysts.

To further reveal the surface chemical composition and valence states of the synthesized samples, the XPS spectra of $\text{Bi}_4\text{O}_5\text{Br}_2$, NiCoP ,

$\text{NiCoP}/\text{Bi}_4\text{O}_5\text{Br}_2$ were analyzed as shown in Fig. 2, where all the elements of Bi, O, Br, Ni, Co, and P are detected in the high-resolution XPS spectra of photocatalysts. The two signals at 164.2 and 158.9 eV in Fig. 2a severally correspond to the $\text{Bi } 4f_{5/2}$ and $\text{Bi } 4f_{7/2}$ orbitals of Bi^{3+} species [29]. As to the O 1s spectrum in Fig. 2b, the peak at 531.4 and 530.0 eV can be ascribed to adsorbed oxygen and lattice O species, respectively. The peak intensity of adsorbed oxygen in $\text{NiCoP}/\text{Bi}_4\text{O}_5\text{Br}_2$ composite is stronger than that of pristine $\text{Bi}_4\text{O}_5\text{Br}_2$, revealing the existence of more adsorbed oxygen species and possibly producing more oxidized radicals [34]. Besides, the two peaks at 69.4 and 68.2 eV are attributed to $\text{Br } 3d_{3/2}$ and $\text{Br } 3d_{5/2}$ of Br^- (Fig. 2c). In addition, as displayed in Fig. 2d, the binding energies of 861.3, 855.8, and 852.7 eV are endorsed to the satellite peak, oxidized nickel species (Ni^{2+}), and Ni^{3+} of the Ni 2p in NiCoP compound, respectively [28]. Similarly, the peaks positioned at 798.0 and 781.9 eV in Fig. 2e of Co 2p are related to the Co $2p_{1/2}$ and Co $2p_{3/2}$ peaks of oxidized cobalt species (Co^{2+}), and the emergence of a peak at 793.8 and 778.6 eV are consigned to the Co $2p_{1/2}$ and Co $2p_{3/2}$ characteristic peaks of Co^{3+} in NiCoP compound [35], respectively. The two satellite peaks of Co appear at higher binding energies of 803.6 and 786.9 eV [27]. Moreover, the P 2p spectrum of NiCoP exhibits two peaks at 132.7 and 129.3 eV (Fig. 2f), ascribed to P $2p_{1/2}$ and P $2p_{3/2}$ of P^{3-} in metal phosphide [28]. Simultaneously, it is worth noting that the binding energies of Bi 4f, Br 3d, and O 1s signals of $\text{NiCoP}/\text{Bi}_4\text{O}_5\text{Br}_2$ show a decreased shift compared to that of pristine $\text{Bi}_4\text{O}_5\text{Br}_2$, while the binding energies of Ni 2p, Co 2p and P 2p peaks of $\text{NiCoP}/\text{Bi}_4\text{O}_5\text{Br}_2$ are increased in contrast to NiCoP sample. The above results not only indicate that NiCoP nanoparticles were successfully modified on the surface of $\text{Bi}_4\text{O}_5\text{Br}_2$, but also suggest a strong interaction between two compositions and the electrons transfer from NiCoP to $\text{Bi}_4\text{O}_5\text{Br}_2$. Apart from this, similar phenomena are also observed in the XPS spectra of $\text{Ni}_2\text{P}/\text{Bi}_4\text{O}_5\text{Br}_2$ and $\text{Co}_2\text{P}/\text{Bi}_4\text{O}_5\text{Br}_2$ heterojunction as illustrated in Figs. S5–6.

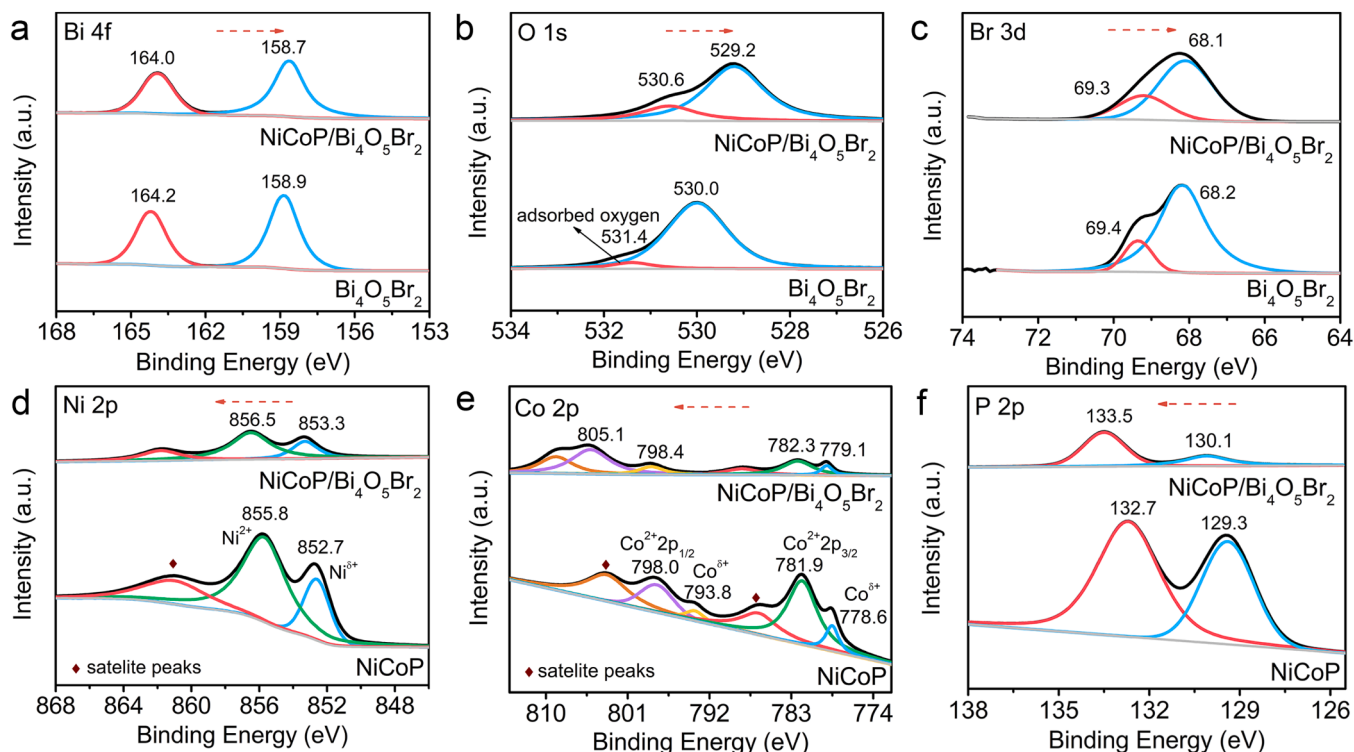


Fig. 2. High-resolution XPS spectra of (a) Bi 4f, (b) O 1s, (c) Br 3d, (d) Ni 2p, (e) Co 2p and (f) P 2p for $\text{Bi}_4\text{O}_5\text{Br}_2$, NiCoP and $\text{NiCoP}/\text{Bi}_4\text{O}_5\text{Br}_2$ catalysts.

3.2. Photocatalytic performance evaluation

3.2.1. Photocatalytic activity for the aerobic degradation of phenolic pollutants

The photocatalytic performance of $\text{Bi}_4\text{O}_5\text{Br}_2$ and TMPs/ $\text{Bi}_4\text{O}_5\text{Br}_2$ was evaluated by aerobic degradation of phenolic pollutants under visible light illumination, including bisphenol A (BPA), p-tert-butylphenol (PTBP), 2,4-dichlorophenol (2,4-DCP) and phenol by using air as the oxidizing agent. As shown in Fig. 3a, pristine $\text{Bi}_4\text{O}_5\text{Br}_2$ presents a poor photocatalytic activity for BPA removal with a degradation rate of only 49.4% at 60 min, it is attributed to the unsatisfactory charge separation efficiency and inadequate ability to activate the molecular oxygen by $\text{Bi}_4\text{O}_5\text{Br}_2$. Notably, after the introduction of TMPs, the degradation efficiency of BPA is significantly enhanced. Both 15% TMPs/ $\text{Bi}_4\text{O}_5\text{Br}_2$ photocatalysts show the optimal degradation rate among the composites with different amounts of Ni_2P , Co_2P , and NiCoP (Fig. S7). When the mass ratios of TMPs were further increased to 20%, the aggregation of TMPs nanoparticles starts to occur, resulting in a slight decrease in degradation rate, so the default amount of TMPs in heterojunction is 15%. In addition, the $\text{NiCoP}/\text{Bi}_4\text{O}_5\text{Br}_2$ exhibits the highest photocatalytic degradation efficiency for BPA, reaching 86.1% of degradation rate and 71.4% of mineralization rate in 60 min (Fig. 3a and Fig. S8). The apparent reaction rate constants (k_{app}) for these reactions were further calculated using a pseudo-first-order model (Fig. S9), and the results were summarized in Table 1. Obviously, the k_{app} of $\text{NiCoP}/\text{Bi}_4\text{O}_5\text{Br}_2$ (0.0371 min^{-1}) for BPA degradation is about 3.4, 1.5, and 1.2 times higher than that of $\text{Bi}_4\text{O}_5\text{Br}_2$ (0.0108 min^{-1}), $\text{Ni}_2\text{P}/\text{Bi}_4\text{O}_5\text{Br}_2$ (0.0250 min^{-1}) and $\text{Co}_2\text{P}/\text{Bi}_4\text{O}_5\text{Br}_2$ (0.0306 min^{-1}), respectively. In order to explore the application scope of photocatalysts, the degradation of PTBP, 2,4-DCP, and phenol are described in Fig. 3b–d and Fig. S8. Unsurprisingly, $\text{NiCoP}/\text{Bi}_4\text{O}_5\text{Br}_2$ photocatalyst exhibits efficient degradation rates of 93.3%, 60.5%, 43.9% and mineralization rates of 81.3%, 52.6%, 38.1% for PTBP, 2,4-DCP, and phenol, respectively. The activity of $\text{NiCoP}/\text{Bi}_4\text{O}_5\text{Br}_2$ is markedly higher than that of $\text{Bi}_4\text{O}_5\text{Br}_2$, $\text{Ni}_2\text{P}/\text{Bi}_4\text{O}_5\text{Br}_2$, and $\text{Co}_2\text{P}/\text{Bi}_4\text{O}_5\text{Br}_2$. Correspondingly, $\text{NiCoP}/\text{Bi}_4\text{O}_5\text{Br}_2$ also

shows the largest k_{app} value among the series of photocatalysts. The above results demonstrate that the introduction of TMPs can effectively enhance the photocatalytic activity of bismuth oxyhalide, and the $\text{NiCoP}/\text{Bi}_4\text{O}_5\text{Br}_2$ heterojunction appears the optimal performance for aerobic degradation of various phenolic pollutants.

Especially, the main intermediates in the BPA degradation by $\text{NiCoP}/\text{Bi}_4\text{O}_5\text{Br}_2$ were identified by liquid chromatography-mass spectrometry (LC-MS, Fig. S10). The proposed degradation pathways confirm the significant roles of $\bullet\text{O}_2^-$ and h^+ in the cleavage of the aromatic ring and C–C bond, and they illustrate the efficient mineralization of phenolic pollutants to form CO_2 and H_2O (Fig. S11, see Supporting Information for related discussions). Moreover, the $\text{NiCoP}/\text{Bi}_4\text{O}_5\text{Br}_2$ photocatalyst was applied for cycling experiments to investigate its recyclability and stability, and the results were displayed in Fig. 3e. The BPA degradation efficiency of $\text{NiCoP}/\text{Bi}_4\text{O}_5\text{Br}_2$ was still maintained at nearly 85.4% after three repeated tests. Furthermore, comparing the XRD patterns before and after the cycling experiment (Fig. 3f), it is found that the crystal structure of the photocatalyst is almost the same as the fresh one, indicating the high stability of $\text{NiCoP}/\text{Bi}_4\text{O}_5\text{Br}_2$ during the photocatalytic process. Therefore, $\text{NiCoP}/\text{Bi}_4\text{O}_5\text{Br}_2$, as an efficient and sustainable photocatalyst, has long-term application potential in wastewater remediation.

3.2.2. Effect of environmental factors on photocatalytic performance

In practice, various inorganic ions exist in the real wastewater, which would produce a negative influence on the treatment of pollutants. As shown in Fig. 4a, the effect of different cations was firstly investigated by adding KCl, NaCl, and MgCl_2 salts, and no reduction of degradation efficiency is found, suggesting the excellent tolerance of $\text{NiCoP}/\text{Bi}_4\text{O}_5\text{Br}_2$ photocatalyst for the common cations. To further reveal the influence of anions on photocatalytic performance, the potassium salts of Cl^- , SO_4^{2-} , and NO_3^- at a concentration of 0.02 M was adopted because K^+ has been proven to show a negligible effect on the reaction [36]. As demonstrated in Fig. 4b, the presence of Cl^- does not influence BPA degradation, and the addition of NO_3^- shows slight inhibition of the

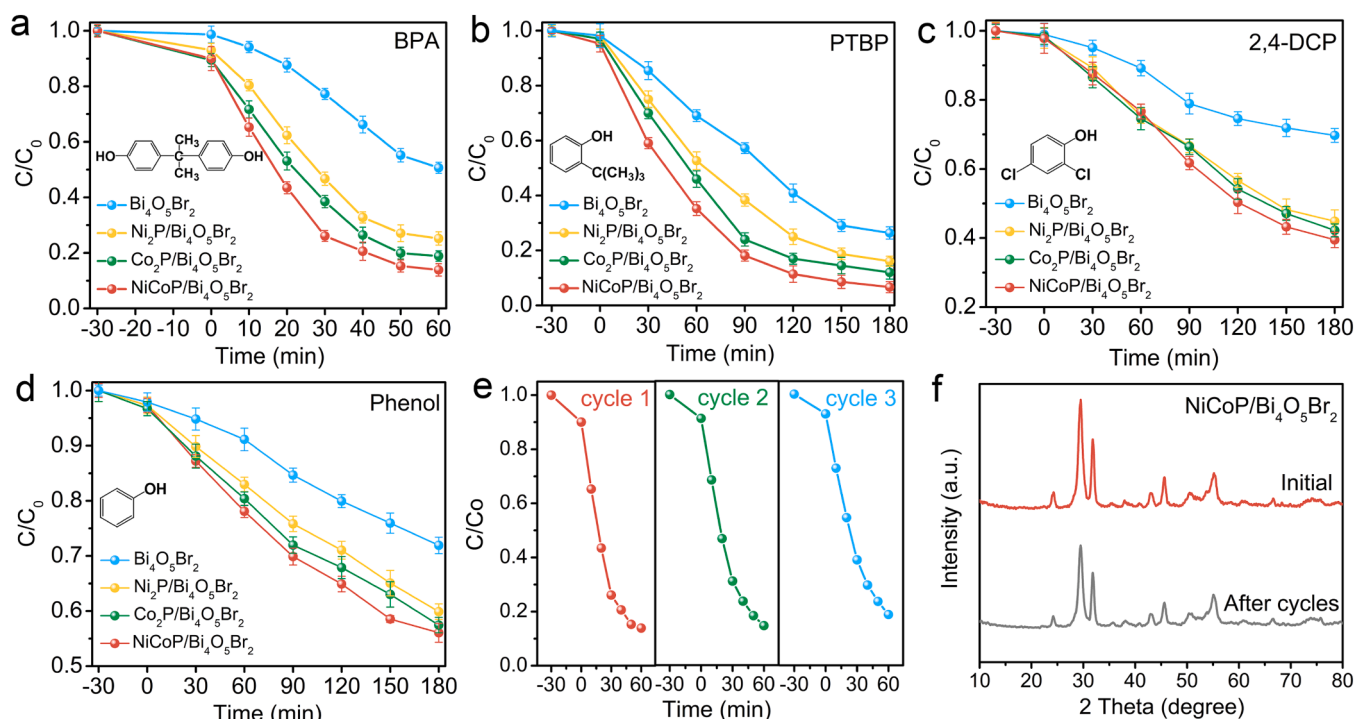
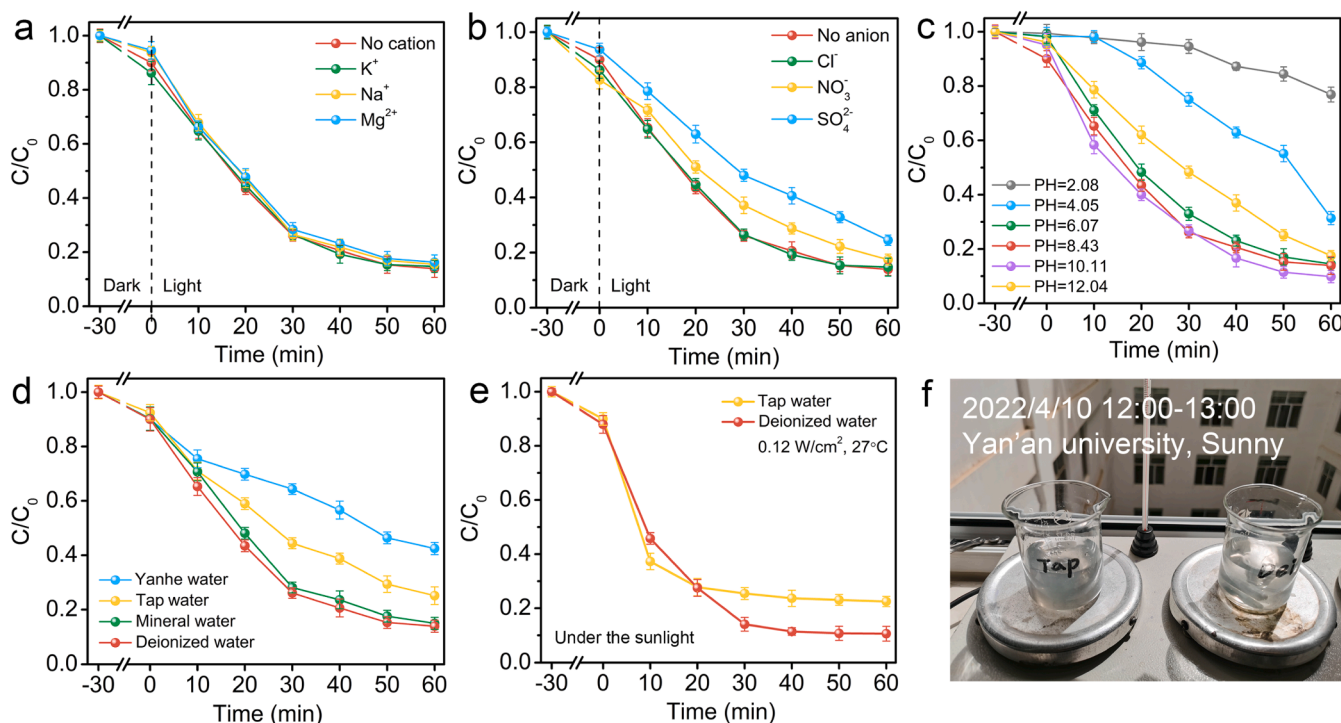


Fig. 3. Photocatalytic activity of $\text{Bi}_4\text{O}_5\text{Br}_2$, $\text{Ni}_2\text{P}/\text{Bi}_4\text{O}_5\text{Br}_2$, $\text{Co}_2\text{P}/\text{Bi}_4\text{O}_5\text{Br}_2$, and $\text{NiCoP}/\text{Bi}_4\text{O}_5\text{Br}_2$ catalysts for the degradation of (a) BPA, (b) PTBP, (c) 2,4-DCP and (d) phenol pollutants under visible light illumination. (e) Recycling experiments of $\text{NiCoP}/\text{Bi}_4\text{O}_5\text{Br}_2$ photocatalyst for BPA degradation. (f) XRD patterns of $\text{NiCoP}/\text{Bi}_4\text{O}_5\text{Br}_2$ before and after cycle experiments.

Table 1Photocatalytic degradation efficiency and apparent reaction rate constant of Bi₄O₅Br₂, Ni₂P/Bi₄O₅Br₂, Co₂P/Bi₄O₅Br₂, and NiCoP/Bi₄O₅Br₂ for different phenols.

Pollutants	Bi ₄ O ₅ Br ₂		Ni ₂ P/Bi ₄ O ₅ Br ₂		Co ₂ P/Bi ₄ O ₅ Br ₂		NiCoP/Bi ₄ O ₅ Br ₂	
	η (%)	k_{app}^{-1} (min)	η (%)	k_{app}^{-1} (min)	η (%)	k_{app}^{-1} (min)	η (%)	k_{app}^{-1} (min)
BPA	49.4	0.0108	74.8	0.0250	81.1	0.0306	86.1	0.0371
PTBP	79.1	0.00744	83.9	0.0107	88.0	0.0131	93.3	0.0165
2,4-DCP	33.3	0.00219	55.1	0.00462	57.8	0.00489	60.5	0.00536
Phenol	28.1	0.00167	40.1	0.00269	42.5	0.00294	43.9	0.00330

* η is the degradation efficiency of phenolic pollutants.**Fig. 4.** The effects of (a) inorganic cations, (b) anions, (c) pH value, and (d) environmental waters for photocatalytic degradation of BPA by NiCoP/Bi₄O₅Br₂ catalyst under visible light illumination. (e–f) Photocatalytic performances of NiCoP/Bi₄O₅Br₂ in tap or deionized water under outdoor sunlight toward the degradation of BPA.

removal of BPA. As for SO_4^{2-} , a decreased photocatalytic activity is observed owing to its trapping effect for the active radical [37].

The influence of pH value on the degradation of BPA was further investigated as shown in Fig. 4c. The initial pH of the BPA solution was altered by adding 0.2 M of HCl or NaOH. It can be found that the adsorption and removal efficiency of BPA improves steadily when the pH value rises from 2.08 to 10.11, indicating that the weak alkaline condition is beneficial to BPA degradation. This is because the optimal pH of 10.11 closes to the dissociation constant (pK_a) of BPA (10.3), which results in the highest H-abstraction rates of various phenolics [38]. However, as the pH exceeds the pK_a value of BPA, excessive OH^- leads to the electrostatic repulsive forces between BPA anion ($-O-C_{15}H_{14}-O-$) and negatively charged catalysts surface [39], resulting in poor efficiency of BPA degradation.

Subsequently, to deeply investigate the practical application of prepared NiCoP/Bi₄O₅Br₂ photocatalyst, different mediums of BPA solution were performed for activity comparison, including deionized water, mineral water (Nongfu Spring: Ca^{2+} , Mg^{2+} , K^+ , Na^+ , SiO_3^{2-} , pH=7.3 \pm 0.5), tap water (Yan'an water supply company: Na^+ , K^+ , Mg^{2+} , Ca^{2+} , Fe^{3+} , Cl^- , NO_3^- , SO_4^{2-} , trace organic substances and microorganisms, etc) and river water (Yanhe river: inorganic mineral, natural organic matters, bacteria, etc; filtration is performed to remove solid particle before use). As displayed in Fig. 4d, it was found that the degradation of BPA can still reach up to 85.0% when mineral water is used, while the

photocatalytic activity of NiCoP/Bi₄O₅Br₂ is decreased to some degree by using tap water and river water. Under these situations, there is a competitive reaction between BPA and organic matters contained in the tap/river water. Besides, the coexisting anions can capture and consume the photogenerated active radicals, further inhibiting the degradation of BPA [40]. Therefore, moderate pretreatment of wastewater is essential for phenolic pollutants removal with NiCoP/Bi₄O₅Br₂ photocatalyst.

3.2.3. Photocatalytic performance under outdoor sunlight

To further explore the applicability of NiCoP/Bi₄O₅Br₂ in practical application, its photocatalytic performance for BPA degradation was investigated by using deionized water and tap water under outdoor sunlight (the optical power is ca. 0.12 W/cm², and the environment temperature is 27 °C). As recorded in Fig. 4e–f, the degradation rate of BPA can satisfyingly reach 86.1% in only 30 min, and finally achieve 89.4% after 60 min when using deionized water as a reaction medium. Moreover, the photocatalytic activity of NiCoP/Bi₄O₅Br₂ in tap water still can reach 77.5%, these performances under natural sunlight compare favorably with that of using a Xe lamp as the light source. The above results demonstrate the good potential of NiCoP/Bi₄O₅Br₂ catalyst for practical application in wastewater treatment.

3.3. Proposed photocatalytic enhanced mechanism

3.3.1. Active species in the photocatalytic aerobic reaction process

To determine the mechanism of photocatalytic aerobic degradation over NiCoP/Bi₄O₅Br₂ heterojunction, a series of active species capture experiments were performed. To this end, reagent isopropanol (IPA), ammonium oxalate (AO), and p-benzoquinone (BQ) were selected as the scavengers for $\bullet\text{OH}$, h^+ and $\bullet\text{O}_2^-$ radical [41], respectively. As displayed in Fig. 5a, the introduction of IPA has no obvious effect on BPA photodegradation efficiency, while the addition of AO and BQ greatly inhibits photocatalytic activity. The results display that the predominant active species are h^+ , followed by $\bullet\text{O}_2^-$ species. Notably, compared with pure Bi₄O₅Br₂, the role of $\bullet\text{O}_2^-$ becomes more significant after the load of the TMPs, suggesting that the introduction of TMPs can improve the yield of $\bullet\text{O}_2^-$ over TMPs/Bi₄O₅Br₂. Simultaneously, the production of $\bullet\text{O}_2^-$ radicals was further validated by EPR measurement. Fig. 5b shows the increased peak intensity of the DMPO- $\bullet\text{O}_2^-$ signal as the order of Bi₄O₅Br₂, Ni₂P/Bi₄O₅Br₂, Co₂P/Bi₄O₅Br₂, and NiCoP/Bi₄O₅Br₂, which further indicates that NiCoP/Bi₄O₅Br₂ possesses strongest ability to activate molecular oxygen and generate $\bullet\text{O}_2^-$ radicals. Moreover, TEMPO could act as scavengers of h^+ in the photocatalytic process, and the weaker signal intensity of TEMPO indicates a higher concentration of h^+ [42,43]. As depicted in Fig. 5c, the pure Bi₄O₅Br₂ sample exhibits a strong TEMPO signal intensity, while NiCoP/Bi₄O₅Br₂ shows evident decreased intensity of TEMPO signal during the same period. The sequence of the TEMPO signal indicates that the construction of NiCoP/Bi₄O₅Br₂ heterojunction can increase the active hole concentration. In contrast, the intensity of the DMPO- $\bullet\text{OH}$ signal is very weak as detected by EPR measurement (Fig. S12). Therefore, it can be concluded that the enhanced photocatalytic activity for NiCoP/Bi₄O₅Br₂ heterojunction derives from the increased oxidative active species of h^+ and $\bullet\text{O}_2^-$ during the reaction upon the modification of NiCoP loading.

3.3.2. Charge transfer mechanism for promoting the concentration of active species

According to the above research, the enhanced activity of TMPs/Bi₄O₅Br₂ heterojunction comes from the increased h^+ and $\bullet\text{O}_2^-$ concentration, thus the behaviors of photogenerated charge carriers including generation, separation, and transfer in TMPs/Bi₄O₅Br₂ heterojunction were further investigated. Fig. 6a and Fig. S13a display the UV-vis absorption spectra of as-prepared photocatalysts. The pristine Bi₄O₅Br₂ sample possesses an absorption edge of 483 nm, and the black TMPs particles exhibit great light-harvesting capability in the whole range at 200–800 nm. Owing to the broad spectral response and excellent light absorption of TMPs, distinctly improved light absorbance of Ni₂P/Bi₄O₅Br₂, Co₂P/Bi₄O₅Br₂, and NiCoP/Bi₄O₅Br₂ photocatalysts are observed in a range of 400–800 nm compared with pristine Bi₄O₅Br₂, which is beneficial to generate more photogenerated charge carriers. In addition, the energy bandgaps (E_g) of Bi₄O₅Br₂, Ni₂P, Co₂P, and NiCoP semiconductors were calculated based on the Tauc's plot of $(\alpha h\nu)^{n/2}$

versus $h\nu$ ($n = 1$ for Bi₄O₅Br₂, $n = 4$ for TMPs) [44], which are estimated to be 2.54, 1.35, 1.30 and 1.26 eV, respectively (Fig. 6b and Fig. S13 b–c). In addition, the Mott-Schottky plots of the above samples were measured at frequencies of 800 and 1000 Hz (Fig. 6c–d and Fig. S13 d–e). The flat-band potentials (E_{fb}) of Bi₄O₅Br₂, Ni₂P, Co₂P, and NiCoP are located at -0.23 , -1.07 , -1.11 , and -1.19 V vs. Ag/AgCl electrode, which are equal to -0.03 , -0.87 , -0.91 and -0.99 V vs. normal hydrogen electrode (NHE), respectively. Since Bi₄O₅Br₂ and above TMPs belong to n-type semiconductors due to the positive slopes of Mott-Schottky curves, the E_{fb} is comparable to the equilibrium Fermi level (E_{F}), and the conduction band potentials (E_{CB}) are accepted to be negative by 0.2 V relative to the E_{F} [44]. Therefore, the E_{CB} of Bi₄O₅Br₂, Ni₂P, Co₂P, and NiCoP are estimated to be -0.23 , -1.07 , -1.11 , and -1.19 V vs. NHE, then the valence band potentials (E_{VB}) are calculated to be 2.31, 0.28, 0.19 and 0.07 V, respectively. The corresponding schematic band structures for the Bi₄O₅Br₂, Ni₂P, Co₂P, and NiCoP photocatalysts are portrayed in Fig. S14.

Based on the band positions described above, the transfer of photo-generated charge carriers between Bi₄O₅Br₂ and TMPs follows either the type-II or S-scheme mechanism. The NiCoP/Bi₄O₅Br₂ heterojunction was selected as the example to reveal the charge transfer mechanism. According to the type-II heterojunction mechanism, the photogenerated electrons on the CB of NiCoP transfer to the CB of Bi₄O₅Br₂. However, O₂ cannot be reduced to $\bullet\text{O}_2^-$ by the photogenerated electrons in CB of Bi₄O₅Br₂, because the E_{CB} of Bi₄O₅Br₂ (-0.23 V vs NHE) is lower than $E^0(\text{O}_2/\bullet\text{O}_2^-)$ (-0.33 V vs NHE) [45]. Meanwhile, the result of EPR also verified the insufficient ability of Bi₄O₅Br₂ for producing $\bullet\text{O}_2^-$, indicating that the charge transfer in NiCoP/Bi₄O₅Br₂ prefers to be an S-scheme mechanism rather than a type-II mechanism.

In order to confirm the S-scheme charge transfer mechanism in NiCoP/Bi₄O₅Br₂ heterojunction, DFT simulations were conducted to obtain the work functions of two components. According to the calculated average potential profile of Bi₄O₅Br₂ and NiCoP (Fig. 6e–f), the work functions were calculated to be 5.40 and 4.84 eV, respectively. Theoretically, as shown in Fig. 6g, the electrons of NiCoP should spontaneously migrate to Bi₄O₅Br₂ at the interface of heterojunction after the contact, which is consistent with the shift of binding energies in XPS spectra (Fig. 2). As a result, the energy bands of Bi₄O₅Br₂ bend upward, while the energy bands of NiCoP bend downward until achieving an equilibrium of Fermi level, a strong built-in electric field with direction from NiCoP to Bi₄O₅Br₂ is established in the space charge region between the heterojunction. Another important evidence for the S-scheme mechanism is the charge transfer route of photogenerated electrons and holes in heterojunction under light irradiation, thereby the in-situ XPS of NiCoP/Bi₄O₅Br₂ was measured for this point. As observed in Fig. 7a–f, the signals of Ni 4f, O 1s, and Br 3d of NiCoP/Bi₄O₅Br₂ heterojunction under ultraviolet light illumination are positively shifted about 0.3–0.4 eV in contrast with those of darkness. Conversely, the binding energies of Ni 2p, Co 2p, and P 2p are negatively shifted about 0.3–0.4 eV, respectively. The opposite shift of binding energies

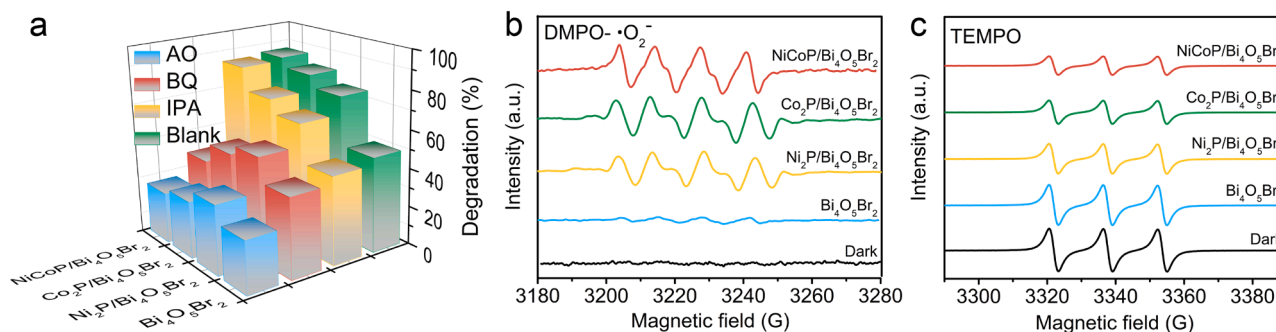


Fig. 5. (a) Trapping experiments of active species during photodegradation of BPA. EPR spectra of (b) DMPO- $\bullet\text{O}_2^-$ and (c) TEMPO over Bi₄O₅Br₂, Ni₂P/Bi₄O₅Br₂, Co₂P/Bi₄O₅Br₂ and NiCoP/Bi₄O₅Br₂ samples under dark and light irradiation.

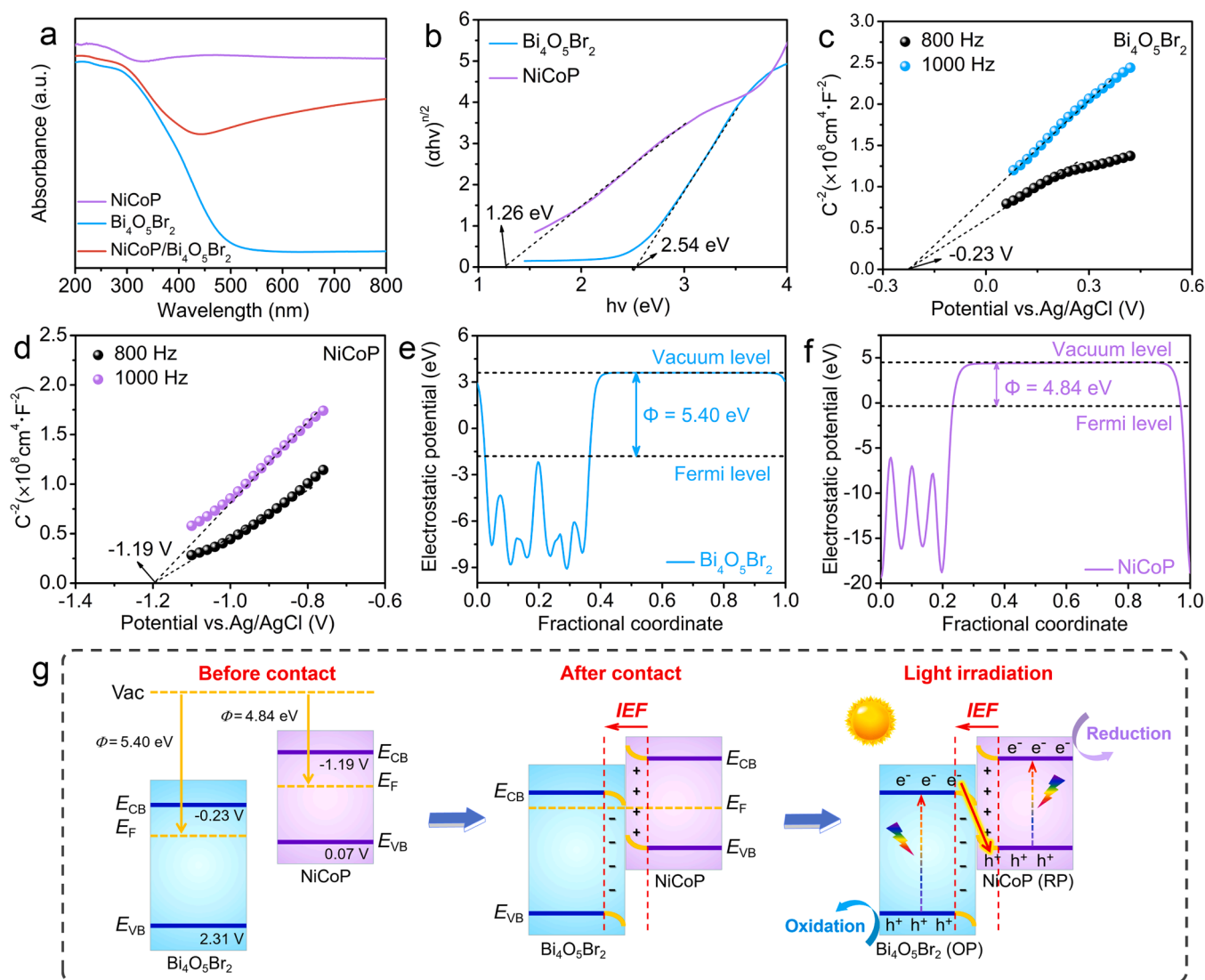


Fig. 6. (a) UV-vis absorption spectra of Bi₄O₅Br₂, NiCoP, and NiCoP/Bi₄O₅Br₂ photocatalysts. (b) Optical bandgaps and (c-d) Mott-Schottky plots and (e-f) calculated work function of Bi₄O₅Br₂ and NiCoP. (g) Schematic illustration of energy band structure configurations of NiCoP/Bi₄O₅Br₂ heterojunction: before contact, after contact, and under light irradiation for S-scheme photogenerated charge transfer.

illustrates the migration of photogenerated electrons from Bi₄O₅Br₂ to NiCoP under light irradiation, verifying the S-scheme mechanism in NiCoP/Bi₄O₅Br₂ heterojunction. Under this circumstance, Bi₄O₅Br₂ is served as an oxidation photocatalyst (OP), and NiCoP is performed as a reduction photocatalyst (RP).

The steady-state photoluminescence (PL) spectra of NiCoP/Bi₄O₅Br₂ exhibits a fluorescence quenching as compared to pristine Bi₄O₅Br₂ (Fig. S15a), demonstrating the effective restriction of photogenerated electron-hole recombination and the existence of non-radiative quenching pathways in heterojunction [46]. Besides, time-resolved photoluminescence (TRPL) decay spectroscopy (Fig. S15b and Table S1) is employed to probe the lifetime of photogenerated charge carriers. The average emission lifetime (τ) of NiCoP/Bi₄O₅Br₂ (0.78 ns) is significantly longer than that of Bi₄O₅Br₂ (0.53 ns), which is in line with the result of steady-state PL. Furthermore, the transient photocurrent density of NiCoP/Bi₄O₅Br₂ photocatalyst is almost 4.72 times higher than that of Bi₄O₅Br₂ (Fig. 7g), revealing the enhanced charge separation and charge transfer kinetics in NiCoP/Bi₄O₅Br₂. Moreover, NiCoP/Bi₄O₅Br₂ presents a much smaller arc radius than Bi₄O₅Br₂ in the electrochemical impedance spectrum (EIS) Nyquist plots (Fig. S15c), indicating the much lower charge transfer impedance of

NiCoP/Bi₄O₅Br₂. It is attributed to the superior electrical conductivity and charge mobility of NiCoP [47]. All results demonstrate that the NiCoP modification can promote the charge dynamics of heterojunction by reducing the surface charge recombination and enhancing the interfacial charge transfer.

Based on the above analyses, the enhanced S-scheme reaction mechanism of NiCoP/Bi₄O₅Br₂ heterojunction for aerobic degradation of phenolic pollutants was illustrated in Fig. 7h. Owing to the narrow bandgap and excellent charge conductivity of NiCoP, the light absorption and charge separation efficiency of NiCoP/Bi₄O₅Br₂ are remarkably promoted, thus increasing the concentration of active photogenerated holes and electrons during the photocatalytic reaction. Specifically, the useless photogenerated electrons in the CB of Bi₄O₅Br₂ are inclined to recombine with the holes in the VB of NiCoP under the force of interface electric field, band bending, and Coulombic attraction [48,49], while the photogenerated electrons of NiCoP with strong reduction potential (-1.09 V) are preserved to activate O₂ and produce $\bullet\text{O}_2^-$ radicals. In the meantime, the trapping of electrons by NiCoP also promotes the accumulation of powerful photogenerated holes (h^+) in the VB of Bi₄O₅Br₂, so the active h^+ and $\bullet\text{O}_2^-$ species with increased concentration are provided for the degradation of phenolic pollutants, resulting in the

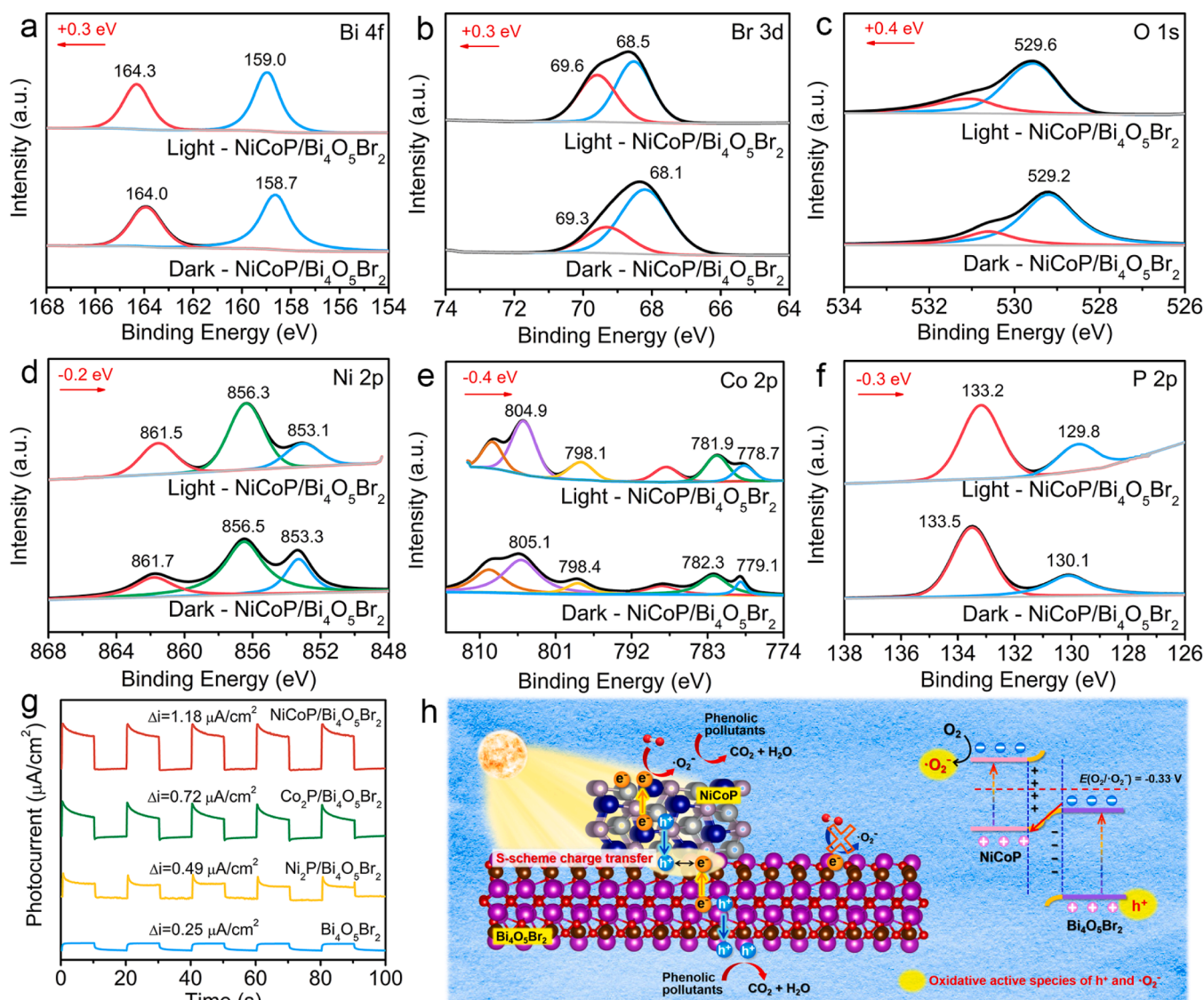


Fig. 7. (a–f) High-resolution XPS spectra of NiCoP/Bi₄O₅Br₂ under dark and ultraviolet light irradiation. (g) Transient photocurrent spectra of photocatalysts. (h) Schematic illustration of charge carrier migration and photocatalytic reaction mechanism of S-scheme NiCoP/Bi₄O₅Br₂ heterojunction for aerobic degradation of phenolic pollutants.

enhanced photogenerated charge kinetic efficiency and photocatalytic performance. Since the properties of the similar materials, the Ni₂P/Bi₄O₅Br₂ and Co₂P/Bi₄O₅Br₂ display the same S-scheme reaction mechanism. However, as shown in Fig. S16, the work function of NiCoP is smaller than that of Ni₂P (5.03 eV) and Co₂P (4.86 eV), which means that the ground-state electrons in dual metal NiCoP have higher energy and can escape from the surface more easily, allowing them to participate in oxygen activation [50]. Besides, NiCoP has a higher CB potential, and the NiCoP/Bi₄O₅Br₂ heterojunction shows more efficient charge separation efficiency compared to Ni₂P/Bi₄O₅Br₂ and Co₂P/Bi₄O₅Br₂ samples as recorded by PL, TRPL, photocurrent measurements, and EIS, all the results refer to the superior photocatalytic activity of NiCoP/Bi₄O₅Br₂.

3.3.3. Mechanism study of promoting oxygen activation

Except for the strong redox potentials and efficient charge separation, the active site of TMPs for O₂ activation is another crucial factor for producing more $\cdot\text{O}_2^-$ radicals in the removal of phenolic pollutants. It is known that the formation of $\cdot\text{O}_2^-$ includes two steps, i) the adsorption of O₂ onto the surface active site of catalyst, and ii) the reduction of

adsorbed O₂ by photogenerated electrons under light irradiation [51]. To identify the O₂ adsorption behavior of Bi₄O₅Br₂ and TMPs, the first-principles calculations of O₂ adsorption energy (E_{ads}) and charge density difference are performed. Models of adsorbed O₂ molecules on the surface of Bi₄O₅Br₂, Ni₂P, Co₂P, and NiCoP active sites after geometry optimization are simulated in Fig. 8. For the pristine Bi₄O₅Br₂, the E_{ads} of O₂ was calculated to be only -0.44 eV . In contrast, the E_{ads} of O₂ on series of Ni₂P, Co₂P, and NiCoP were calculated to be -2.35 , -2.52 , and -2.77 eV , respectively. Obviously, NiCoP exhibits the best affinity with O₂ over Bi₄O₅Br₂, Ni₂P, and Co₂P from the perspective of thermodynamics. The result indicates that NiCoP is the active site for O₂ activation in NiCoP/Bi₄O₅Br₂ heterojunction.

The chemisorption of O₂ is accompanied by electron transfer and change of O–O bond length. According to the calculation of charge density difference and Bader number between the adsorbed O₂ and the catalysts (Fig. 8 and Table S2), the electrons transferred from adsorption sites to O₂ are 0.32, 1.12, 0.62, and 0.83 e for Bi₄O₅Br₂ and Ni₂P, Co₂P and NiCoP, respectively. The corresponding O–O bond length of the adsorbed O₂ molecule on different substrates is 1.27, 1.48, 1.32, and 1.43 Å, respectively (O–O bond length of pristine O₂ is 1.24 Å). It is

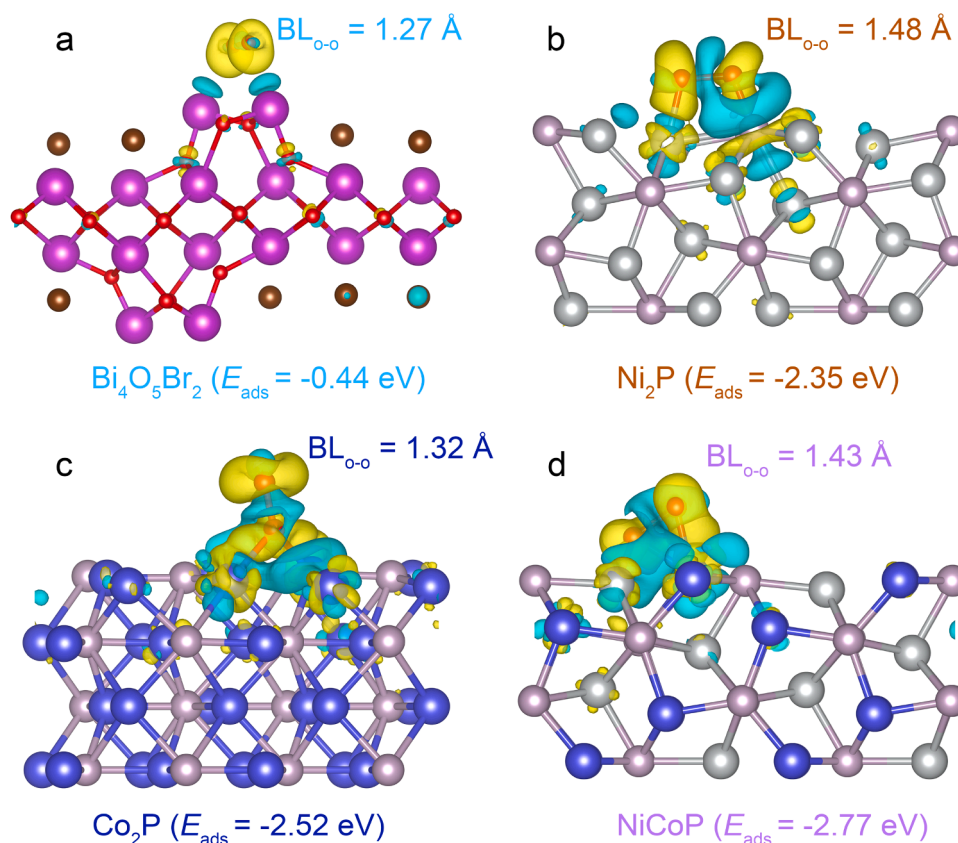


Fig. 8. The configuration and charge density difference of (a) $Bi_4O_5Br_2$, (b) Ni_2P , (c) Co_2P , and (d) $NiCoP$ surface with O_2 adsorption, the yellow and blue isosurfaces represent charge accumulation and depletion in the space, respectively.

noted that the charge transfer and change of O–O bond length is closely related to the adsorption configurations (Fig. S17). $Bi_4O_5Br_2$ displays weak adsorption of O_2 without stable chemical bonding, the negligible extension of O–O bond length reflects the inadequate ability of $Bi_4O_5Br_2$ to activate the molecular oxygen. In contrast, the elongated O–O bond lengths on TMPs substrates demonstrate the enhanced activation of O_2 due to more electron donation [52]. Specifically, Ni_2P shows bridge-type adsorption for O_2 , resulting in the longer O–O bond length due to the stronger molecular pull force. Co_2P exhibits top-type adsorption with relatively weak interaction. Besides, a square configuration of O_2 adsorption with multiple bonds connection is observed for $NiCoP$, so the O–O bond length is intermediate. In contrast, dual metals $NiCoP$ possesses advantages in geometric and electrical effects, which can create coordinatively unsaturated sites for strong interactions with O_2 . The multiple bonds connection is beneficial for the subsequent photoreduction of adsorbed O_2 by photogenerated electrons from $NiCoP$. According to these results, it can be concluded that $NiCoP/Bi_4O_5Br_2$ has superiority in the activation of O_2 compared with other samples owing to the stronger adsorption ability of $NiCoP$.

More experimental insights were conducted to determine the rationale for the enhanced photocatalytic O_2 adsorption and reduction of $NiCoP/Bi_4O_5Br_2$. As a premise, all the photocatalysts are stable in the 100–600 °C temperature range based on the thermogravimetric analysis (Fig. S18). Then, the O_2 -TPD experiments demonstrate the chemisorption ability of photocatalysts to O_2 molecules. As illustrated in Fig. 10a, compared with the single metal phosphides of Ni_2P and Co_2P , the O_2 desorption peak intensity of $NiCoP$ is significantly stronger and the desorbed peak appears at the higher temperature of 295.5 °C. It directly proves that dual metal $NiCoP$ has more adsorption quantity and stronger interactions with O_2 . Correspondingly, the TMPs/ $Bi_4O_5Br_2$ composites display a much better affinity with O_2 compared with the pure $Bi_4O_5Br_2$ sample (Fig. 9b), the strongest TPD signals at high temperatures of

322.6 °C and 562.1 °C achieved by $NiCoP/Bi_4O_5Br_2$ indicate its best chemical adsorption capacity based on the introduction of $NiCoP$. Moreover, as evidenced by electrochemical oxygen reduction curves (Fig. S19), $NiCoP/Bi_4O_5Br_2$ exhibits the most positive onset potential compared with other samples as expected, suggesting that $NiCoP/Bi_4O_5Br_2$ is more favorable for O_2 reduction [53]. Furthermore, NBT was used as an indicator to detect the generated amount of $\bullet O_2^-$ in photocatalytic reaction. The yellow NBT can specifically react with $\bullet O_2^-$ to form blue formazan, and the yields of $\bullet O_2^-$ are determined to be four times compared to the consumption of NBT. As shown in Fig. 9c–f, $NiCoP/Bi_4O_5Br_2$ displays the best photocatalytic activity for the transformation of NBT, the corresponding $\bullet O_2^-$ production rates of $Bi_4O_5Br_2$, $Ni_2P/Bi_4O_5Br_2$, $Co_2P/Bi_4O_5Br_2$, and $NiCoP/Bi_4O_5Br_2$ samples are ca. 4.35, 22.32, 30.46 and 38.22 $\mu\text{mol}\cdot\text{L}^{-1}\cdot\text{h}^{-1}$, respectively. The tendency is coinciding with the results of pollutants degradation and BQ trapping experiments, and the dates further reveal that loading of the $NiCoP$ can boost the formation of $\bullet O_2^-$ radicals.

4. Conclusions

In summary, we designed a simple liquid assembly method to load bifunctional TMPs cocatalysts (Ni_2P , Co_2P , and $NiCoP$) on $Bi_4O_5Br_2$ nanosheets, 15% $NiCoP/Bi_4O_5Br_2$ heterojunction shows the most excellent photocatalytic activity for aerobic degradation of phenolic pollutants in various water matrix under visible light. The trapping experiments demonstrate that both photogenerated holes (h^+) and superoxide radical ($\bullet O_2^-$) are the decisive oxidative active species in degrading reactions. Furthermore, theoretical simulations and experimental analyses confirm that the introduction of $NiCoP$ can induce an S-scheme charge transfer mechanism in $NiCoP/Bi_4O_5Br_2$, resulting in more efficient separation of photogenerated charge carriers and increased concentration of active h^+ . Meanwhile, $NiCoP$ shows stronger

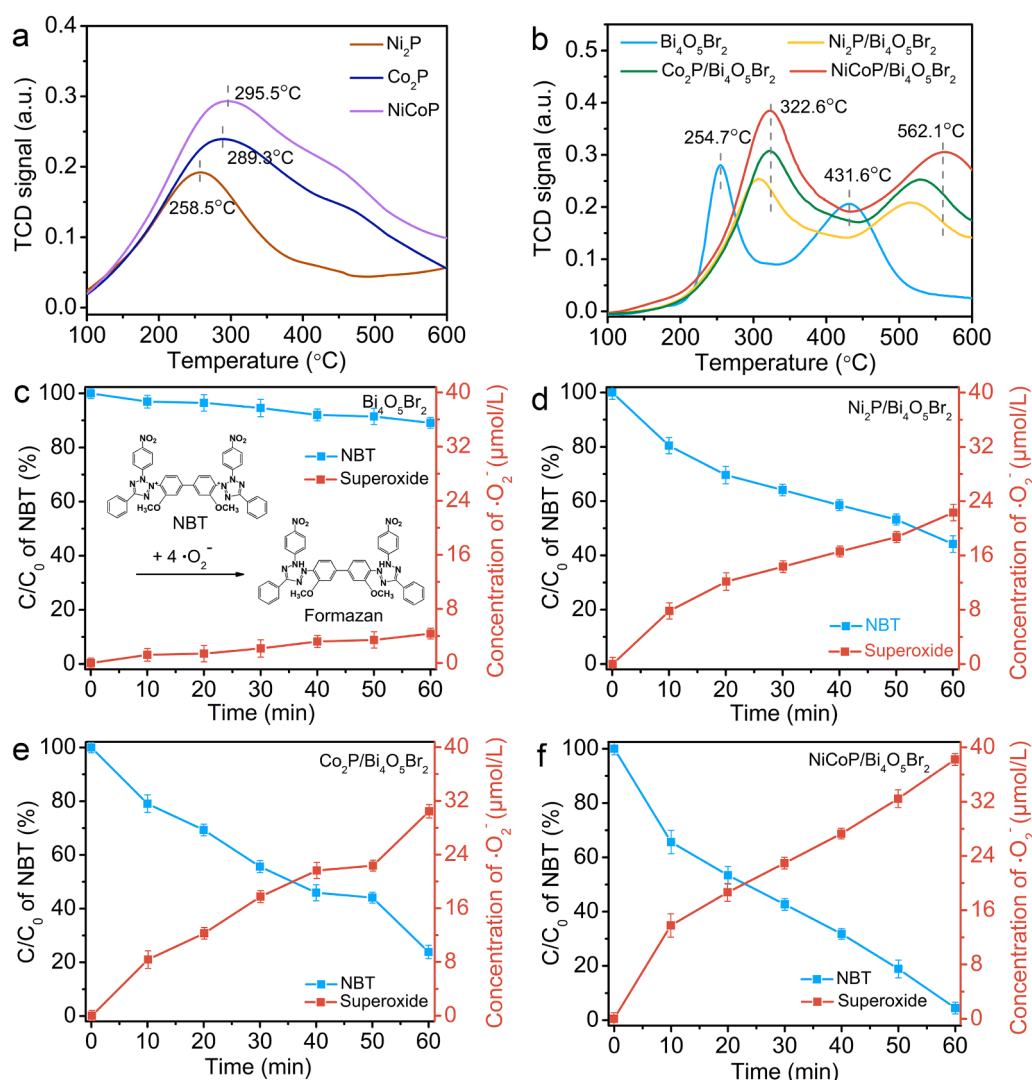


Fig. 9. (a–b) The O₂-TPD curves of different photocatalysts. (c–f) Variation of NBT concentration and •O₂⁻ concentration in NBT degradation process by Bi₄O₅Br₂, Ni₂P/Bi₄O₅Br₂, Co₂P/Bi₄O₅Br₂, and NiCoP/Bi₄O₅Br₂ samples.

reduction potential and superior O₂ activation ability than Ni₂P and Co₂P, thus leading to generating more active •O₂⁻. Therefore, the enhanced photocatalytic activity of NiCoP/Bi₄O₅Br₂ is attributed to the bifunctional effect of NiCoP for boosting holes generation and O₂ activation. This research comes up with new insight for accelerating the generation of oxidative active species and a feasible way for the practical application of photocatalytic aerobic oxidation technology.

CRediT authorship contribution statement

Weijie Yang: Investigation, Formal analysis, Data curation, Writing – original draft. **Kailong Sun:** Investigation, Data curation. **Jun Wan:** Visualization, Writing – review & editing, Funding acquisition. **Jiaqing Liu:** Investigation. **Yang-Ai Ma:** Investigation. **Bicheng Zhu:** Conceptualization, Theoretical simulation, Funding acquisition. **Lin Liu:** Supervision, Funding acquisition. **Feng Fu:** Supervision, Funding acquisition.

Declaration of Competing Interest

The authors declare that they have no known competing financial interests or personal relationships that could have appeared to influence the work reported in this paper.

Data Availability

Data will be made available on request.

Acknowledgements

This work was supported by the National Natural Science Foundation of China (Nos. 21908187, 22169021, 52173065), National Key Research and Development Program of China (2019YFC1905803), Project of Science and Technology Office of Shaanxi Province (2021KJXX-41, 2021JQ-611, 2022GY-176), Special projects for high-level talents of Yan'an city (2019–02).

Appendix A. Supporting information

Supplementary data associated with this article can be found in the online version at [doi:10.1016/j.apcatb.2022.121978](https://doi.org/10.1016/j.apcatb.2022.121978).

References

- [1] Z. Wu, J. Jing, K. Zhang, W. Li, J. Yang, J. Shen, S. Zhang, K. Xu, S. Zhang, Y. Zhu, Epitaxial BiP₅O₁₄ layer on BiOI nanosheets enhancing the photocatalytic degradation of phenol via interfacial internal-electric-field, *Appl. Catal. B Environ.* 307 (2022), 121153.

- [2] S. Zhang, Y. Zhuo, C.I. Ezugwu, C.C. Wang, C. Li, S. Liu, Synergetic molecular oxygen activation and catalytic oxidation of formaldehyde over defective MIL-88B (Fe) nanorods at room temperature, *Environ. Sci. Technol.* 55 (2021) 8341–8350.
- [3] H. Yu, M. Wang, J. Yan, H. Dang, H. Zhu, Y. Liu, M. Wen, G. Li, L. Wu, Complete mineralization of phenolic compounds in visible-light-driven photocatalytic ozonation with single-crystal WO_3 nanosheets: performance and mechanism investigation, *J. Hazard. Mater.* 433 (2022), 128811.
- [4] I. Shafiq, S. Shafique, P. Akhter, G. Abbas, A. Qurashi, M. Hussain, Efficient catalyst development for deep aerobic photocatalytic oxidative desulfurization: recent advances, confines, and outlooks, *Catal. Rev. Sci. Eng.* (2021) 1–46.
- [5] H. Zhan, Q. Zhou, M. Li, R. Zhou, Y. Mao, P. Wang, Photocatalytic O_2 activation and reactive oxygen species evolution by surface B–N bond for organic pollutants degradation, *Appl. Catal. B Environ.* 310 (2022), 121329.
- [6] S. Vinoth, W.J. Ong, A. Pandikumar, Defect engineering of BiOX ($X = \text{Cl}, \text{Br}, \text{I}$) based photocatalysts for energy and environmental applications: current progress and future perspectives, *Coord. Chem. Rev.* 464 (2022), 214541.
- [7] C.W. Siao, W.L.W. Lee, Y.M. Dai, W.H. Chung, J.T. Hung, P.H. Huang, W.Y. Lin, C. Chen, $\text{BiO}_x\text{Cl}_y/\text{BiO}_m\text{Br}_n/\text{BiO}_p\text{I}_q/\text{GO}$ quaternary composites: syntheses and application of visible-light-driven photocatalytic activities, *J. Colloid Interface Sci.* 544 (2019) 25–36.
- [8] J. Wan, W. Yang, J. Liu, K. Sun, L. Liu, F. Fu, Enhancing an internal electric field by a solid solution strategy for steering bulk-charge flow and boosting photocatalytic activity of $\text{Bi}_{24}\text{O}_{31}\text{Cl}_x\text{Br}_{10-x}$, *Chin. J. Catal.* 43 (2022) 485–496.
- [9] M. Xu, J. Yang, C. Sun, L. Liu, Y. Cui, B. Liang, Performance enhancement strategies of bi-based photocatalysts: a review on recent progress, *Chem. Eng. J.* 389 (2020), 124402.
- [10] Y.C. Chou, Y.Y. Lin, C.S. Lu, F.Y. Liu, J.H. Lin, F.H. Chen, C.C. Chen, W.T. Wu, Controlled hydrothermal synthesis of $\text{BiO}_x\text{Cl}_y/\text{BiO}_m\text{Br}_n/\text{g-C}_3\text{N}_4$ composites exhibiting visible-light photocatalytic activity, *J. Environ. Manag.* 297 (2021), 113256.
- [11] X. Chen, Y. Li, Z. Wu, X. Xu, W. Zhu, X. Gao, $\text{Bi}_4\text{O}_5\text{Br}_2$ anchored on Ti_3C_2 MXene with ohmic heterojunction in photocatalytic NH_3 production: insights from combined experimental and theoretical calculations, *J. Colloid Interface Sci.* 602 (2021) 553–562.
- [12] Z.J. Chen, H. Guo, H.Y. Liu, C.G. Niu, D.W. Huang, Y.Y. Yang, C. Liang, L. Li, J. C. Li, Construction of dual S-scheme $\text{Ag}_2\text{CO}_3/\text{Bi}_4\text{O}_5\text{I}_2/\text{g-C}_3\text{N}_4$ heterostructure photocatalyst with enhanced visible-light photocatalytic degradation for tetracycline, *Chem. Eng. J.* 438 (2022), 135471.
- [13] H. Jia, B. Zhang, W. He, Y. Xiang, Z. Zheng, Mechanistic insights into the photoinduced charge carrier dynamics of BiOBr/CdS nanosheet heterojunctions for photovoltaic application, *Nanoscale* 9 (2017) 3180–3187.
- [14] L.F. Hong, R.T. Guo, Y. Yuan, X.Y. Ji, Z.D. Lin, Z.S. Li, W.G. Pan, Recent progress of transition metal phosphides for photocatalytic hydrogen evolution, *ChemSusChem* 14 (2021) 539–557.
- [15] H.L. Jiang, K. Sun, M. Liu, J. Pei, D. Li, C. Ding, K. Wu, Incorporating transition metal phosphides into metal-organic frameworks for enhanced photocatalysis, *Angew. Chem. Int. Ed.* 132 (2020) 22937–22943.
- [16] W. Wang, T. An, G. Li, D. Xia, H. Zhao, J.C. Yu, P.K. Wong, Earth-abundant $\text{Ni}_2\text{P}/\text{g-C}_3\text{N}_4$ lamellar nanohybrids for enhanced photocatalytic hydrogen evolution and bacterial inactivation under visible light irradiation, *Appl. Catal. B Environ.* 217 (2017) 570–580.
- [17] U.J. Eitim, P. Bai, O.M. Gazit, Z. Zhong, Low-temperature heterogeneous oxidation catalysis and molecular oxygen activation, *Catal. Rev.* (2021) 1–187.
- [18] M.M. Montemore, M.A. van Spronsen, R.J. Madix, C.M. Friend, O_2 activation by metal surfaces: implications for bonding and reactivity on heterogeneous catalysts, *Chem. Rev.* 118 (2018) 2816–2862.
- [19] F. Kong, R. Si, N. Chen, Q. Wang, J. Li, G. Yin, M. Gu, J. Wang, L.M. Liu, X. Sun, Origin of hetero-nuclear Au–Co dual atoms for efficient acidic oxygen reduction, *Appl. Catal. B Environ.* 301 (2022), 120782.
- [20] Y. Li, Z. Dong, L. Jiao, Multifunctional transition metal-based phosphides in energy-related electrocatalysis, *Adv. Energy Mater.* 10 (2020), 1902104.
- [21] Y. Shi, M. Li, Y. Yu, B. Zhang, Recent advances in nanostructured transition metal phosphides: synthesis and energy-related applications, *Energy Environ. Sci.* 13 (2020) 4564–4582.
- [22] J.G. Jang, Y.K. Lee, Promotional effect of Ga for Ni_2P catalyst on hydrodesulfurization of 4,6-DMDBT, *Appl. Catal. B Environ.* 250 (2019) 181–188.
- [23] L. Liu, J. Liu, K. Sun, J. Wan, F. Fu, J. Fan, Novel phosphorus-doped Bi_2WO_6 monolayer with oxygen vacancies for superior photocatalytic water detoxication and nitrogen fixation performance, *Chem. Eng. J.* 411 (2021), 128629.
- [24] Z. Wu, J. Shen, N. Ma, Z. Li, M. Wu, D. Xu, S. Zhang, W. Feng, Y. Zhu, $\text{Bi}_4\text{O}_5\text{Br}_2$ nanosheets with vertical aligned facets for efficient visible-light-driven photodegradation of BPA, *Appl. Catal. B Environ.* 286 (2021), 119937.
- [25] S. Surendran, S. Shanmugapriya, A. Sivanantham, S. Shanmugam, R.K. Selvan, Electrospun carbon nanofibers encapsulated with NiCoP : a multifunctional electrode for supercapattery and oxygen reduction, oxygen evolution, and hydrogen evolution reactions, *Adv. Energy Mater.* 8 (2018), 1800555.
- [26] T. Hu, K. Dai, J. Zhang, S. Chen, Noble-metal-free Ni_2P modified step-scheme $\text{SnNb}_2\text{O}_6/\text{CdS}$ -diethylenetriamine for photocatalytic hydrogen production under broadband light irradiation, *Appl. Catal. B Environ.* 269 (2020), 118844.
- [27] H. Liu, J. Guan, S. Yang, Y. Yu, R. Shao, Z. Zhang, M. Dou, F. Wang, Q. Xu, Metal-organic-framework-derived Co_2P nanoparticle/multi-doped porous carbon as a trifunctional electrocatalyst, *Adv. Mater.* 32 (2020), 2003649.
- [28] X. Lv, X. Li, C. Yang, X. Ding, Y. Zhang, Y.Z. Zheng, S. Li, X. Sun, X. Tao, Large-size, porous, ultrathin NiCoP nanosheets for efficient electro/photocatalytic water splitting, *Adv. Funct. Mater.* 30 (2020), 1910830.
- [29] X.A. Dong, Z. Cui, X. Shi, P. Yan, Z. Wang, A.C. Co, F. Dong, Insights into dynamic surface bromide sites in $\text{Bi}_4\text{O}_5\text{Br}_2$ for sustainable N_2 photofixation, *Angew. Chem. Int. Ed.* 61 (2022), e2022009.
- [30] J.X. Liu, R. Li, X. Zu, X.C. Zhang, Y.F. Wang, Y.W. Wang, C.M. Fan, Photocatalytic conversion of nitrogen to ammonia with water on triphase interfaces of hydrophilic-hydrophobic composite $\text{Bi}_4\text{O}_5\text{Br}_2/\text{ZIF-8}$, *Chem. Eng. J.* 371 (2019) 796–803.
- [31] Y.X. Sun, L. Wang, T. Wang, X.Q. Liu, T. Xu, M.B. Wei, L.L. Yang, C.X. Li, Improved photocatalytic activity of $\text{Ni}_2\text{P}/\text{NiCo-LDH}$ composites via a Co–P bond charge transfer channel to degrade tetracycline under visible light, *J. Alloy. Compd.* 852 (2021), 156963.
- [32] F.T. Yi, J.Q. Ma, C.W. Lin, L.Y. Wang, H.N. Zhang, Y.X. Qian, K.F. Zhang, Insights into the enhanced adsorption/photocatalysis mechanism of a $\text{Bi}_4\text{O}_5\text{Br}_2/\text{g-C}_3\text{N}_4$ nanosheet, *J. Alloy. Compd.* 821 (2020), 153557.
- [33] X.S. Zhao, Y.Y. You, S.B. Huang, Y.X. Wu, Y.Y. Ma, G. Zhang, Z.H. Zhang, Z-scheme photocatalytic production of hydrogen peroxide over $\text{Bi}_4\text{O}_5\text{Br}_2/\text{g-C}_3\text{N}_4$ heterostructure under visible light, *Appl. Catal. B Environ.* 278 (2020), 119251.
- [34] F. Chang, W. Yan, X. Wang, S. Peng, S. Li, X. Hu, Strengthened photocatalytic removal of bisphenol A by robust 3D hierarchical n-p heterojunctions $\text{Bi}_4\text{O}_5\text{Br}_2\text{-MnO}_2$ via boosting oxidative radicals generation, *Chem. Eng. J.* 428 (2022), 131223.
- [35] J. Hu, T. Yang, X. Yang, J. Qu, Y. Cai, C.M. Li, Highly selective and efficient solar-light-driven CO_2 conversion with an ambient-Stable $2\text{D}/2\text{D}$ $\text{Co}_2\text{P@BP/g-C}_3\text{N}_4$ heterojunction, *Small* 18 (2022), 2105376.
- [36] H. Ming, D. Wei, Y. Yang, B. Chen, C. Yang, J. Zhang, Y. Hou, Photocatalytic activation of peroxymonosulfate by carbon quantum dots functionalized carbon nitride for efficient degradation of bisphenol A under visible-light irradiation, *Chem. Eng. J.* 424 (2021), 130296.
- [37] D. Huang, J. Li, G. Zeng, W. Xue, S. Chen, Z. Li, R. Deng, Y. Yang, M. Cheng, Facile construction of hierarchical flower-like Z-scheme $\text{AgBr}/\text{Bi}_2\text{WO}_6$ photocatalysts for effective removal of tetracycline: Degradation pathways and mechanism, *Chem. Eng. J.* 375 (2019), 121991.
- [38] T.Y. Liu, C. Wang, Y.Z. Han, C. Bai, H.T. Ren, Y. Liu, X. Han, Oxidative polymerization of bisphenol A (BPA) via H-abstraction by $\text{Bi}_{12}\text{WO}_6$ and persulfate: importance of the surface complexes, *Chem. Eng. J.* 435 (2022), 134816.
- [39] S. Gao, C. Guo, J. Lv, Q. Wang, Y. Zhang, S. Hou, J. Gao, J. Xu, A novel 3D hollow magnetic $\text{Fe}_3\text{O}_4/\text{BiOI}$ heterojunction with enhanced photocatalytic performance for bisphenol A degradation, *Chem. Eng. J.* 307 (2017) 1055–1065.
- [40] S. Ye, M. Yan, X. Tan, J. Liang, G. Zeng, H. Wu, B. Song, C. Zhou, Y. Yang, H. Wang, Facile assembled biochar-based nanocomposite with improved graphitization for efficient photocatalytic activity driven by visible light, *Appl. Catal. B Environ.* 250 (2019) 78–88.
- [41] C.W. Siao, H.L. Chen, L.W. Chen, J.L. Chang, T.W. Yeh, C.C. Chen, Controlled hydrothermal synthesis of bismuth oxychloride/bismuth oxybromide/bismuth oxyiodide composites exhibiting visible-light photocatalytic degradation of 2-hydroxybenzoic acid and crystal violet, *J. Colloid Interface Sci.* 526 (2018) 322–336.
- [42] F. Guo, H. Zhang, H. Li, Z. Shen, Modulating the oxidative active species by regulating the valence of palladium cocatalyst in photocatalytic degradation of ciprofloxacin, *Appl. Catal. B Environ.* 306 (2022), 120192.
- [43] J.L. Shi, R. Chen, H. Hao, C. Wang, X. Lang, 2D sp^2 carbon-conjugated porphyrin covalent organic framework for cooperative photocatalysis with TEMPO, *Angew. Chem. Int. Ed.* 59 (2020) 9088–9093.
- [44] X. Li, W. He, C. Li, B. Song, S. Liu, Synergetic surface modulation of $\text{ZnO}/\text{Pt@ZIF-8}$ hybrid nanorods for enhanced photocatalytic CO_2 valorization, *Appl. Catal. B Environ.* 287 (2021), 119934.
- [45] S. Li, L. Li, Y. Li, L. Dai, C. Liu, Y. Liu, J. Li, J. Lv, P. Li, Bo Wang, Fully conjugated donor–acceptor covalent organic frameworks for photocatalytic oxidative amine coupling and thioamide cyclization, *ACS Catal.* 10 (2020) 8717–8726.
- [46] P. Wang, Z. Shen, Y. Xia, H. Wang, L. Zheng, W. Xi, S. Zhan, Atomic insights for optimum and excess doping in photocatalysis: a case study of few-layer $\text{Cu-ZnIn}_2\text{S}_4$, *Adv. Funct. Mater.* 29 (2019), 1807013.
- [47] L. Bi, X. Gao, L. Zhang, D. Wang, X. Zou, T. Xie, Enhanced photocatalytic hydrogen evolution of $\text{NiCoP}/\text{g-C}_3\text{N}_4$ with improved separation efficiency and charge transfer efficiency, *ChemSusChem* 11 (2018) 276–284.
- [48] Q. Xu, L. Zhang, B. Cheng, J. Fan, J. Yu, S-scheme heterojunction photocatalyst, *Chem* 6 (2020) 1543–1559.
- [49] Q. Xie, W. He, S. Liu, C. Li, J. Zhang, P.K. Wong, Bifunctional S-scheme $\text{g-C}_3\text{N}_4/\text{Bi}/\text{BiVO}_4$ hybrid photocatalysts toward artificial carbon cycling, *Chin. J. Catal.* 41 (2020) 140–153.
- [50] Z. Yang, X. Xia, W. Yang, L. Wang, Y. Liu, Photothermal effect and continuous hot electrons injection synergistically induced enhanced molecular oxygen activation for efficient selective oxidation of benzyl alcohol over plasmonic $\text{W}_{18}\text{O}_{49}/\text{ZnIn}_2\text{S}_4$ photocatalyst, *Appl. Catal. B Environ.* 299 (2021), 120675.
- [51] Z. Wang, Y. Huang, M. Chen, X. Shi, Y. Zhang, J. Cao, W. Ho, S.C. Lee, Roles of N-vacancies over porous $\text{g-C}_3\text{N}_4$ microtubes during photocatalytic NO_x removal, *ACS Appl. Mater. Interface* 11 (2019) 10651–10662.
- [52] T. Gan, J. Yang, D. Morris, X. Chu, P. Zhang, W. Zhang, Y. Zou, W. Yan, S.H. Wei, G. Liu, Electron donation of non-oxide supports boosts O_2 activation on nano-platinum catalysts, *Nat. Commun.* 12 (2021) 2741.
- [53] X. Chu, Y. Qu, A. Zada, L. Bai, Z. Li, F. Yang, L. Zhao, G. Zhang, X. Sun, Z.D. Yang, L. Jing, Ultrathin phosphate-modulated Co phthalocyanine/ $\text{g-C}_3\text{N}_4$ heterojunction photocatalysts with single Co–N₄ (II) sites for efficient O_2 activation, *Adv. Sci.* 7 (2020), 2001543.